**Acar Celik**
Technion—Israel Institute of Technology,
Haifa 32000, Israel
e-mail: acar.celik@campus.technion.ac.il

**Abhijit Mitra**
Technion—Israel Institute of Technology,
Haifa 32000, Israel
e-mail: abhijitmitra@campus.technion.ac.il

**Tapish Agarwal**
Technion—Israel Institute of Technology,
Haifa 32000, Israel
e-mail: tapish@technion.ac.il

**John Clark**
Air Force Research Laboratory,
1950 Fifth Street,
Wright Patterson AFB, OH 45433
e-mail: john.clark.38@us.af.mil

**Ian Jacobi**
Technion—Israel Institute of Technology,
Haifa 32000, Israel
e-mail: ijacobi@technion.ac.il

**Beni Cukurel**[1]
Technion—Israel Institute of Technology,
Haifa 32000, Israel
e-mail: beni@cukurel.org

# Exploring Physics of Acoustic Flow Control Over Airfoils Toward Potential Application to High Work and Lift Turbines

*In this study, acoustic actuation was applied experimentally to massively separated flows on simplified hump geometries, which mimic the pressure distribution over high-work-and-lift low Reynolds airfoils. The acoustic excitation demonstrated significant control over flow separation, resulting in higher relative lift enhancement than standard, localized actuation techniques with similar momentum coefficients. Full-field velocity measurements were used to examine the transient behavior of the actuated flow in order to explain the physical mechanism of separation control. The velocity measurements revealed the presence of a viscous wall mode that organized the vorticity upstream of the separation point. A spatio-temporal correlation analysis found that the generation of these wall modes in the attached flow was the dominant cause of the subsequent reorganization of the separating shear layer and the change in separation dynamics. The importance of wall modes to acoustic flow control mechanism has important implications for the design of new acoustic control strategies for high-speed turbomachinery. Along these lines, the ramifications of this phenomena are explored over geometries, which are designed to approximate flow fields in high-speed turbomachinery. At the conducive Strouhal number, which scale linearly with the square root of Reynolds numbers, up to 22% lift enhancement is observed for excitation amplitudes in the range of ~128 dB, typical to the engine environment. Of the many diverse flow control techniques, acoustics can be effectively employed in low Reynolds turbine blades, which are prone to flow separation in the off-design conditions with the ever increasing demand for higher flow turning.* [DOI: 10.1115/1.4063923]

*Keywords: acoustic flow control, seperation control, wall modes, airfoil lift enhancement*

## 1 Introduction

Efforts to reduce the overall weight and specific fuel consumption of aeroengines often involve increasing turbine blade turning angles to increase the loading on the blades. Unfortunately, this has the effect of generating greater adverse pressure gradients over the airfoils, leading to the possibility of flow separation which causes performance degradation. In order to prevent the separation, a variety of control techniques have been applied, including synthetic jets, bleed-air blowing/suction, dielectric barrier, and discharge actuators, among others [1–6]. These techniques all perturb the flow locally, near the point of separation, in order to delay or prevent the separation by organizing the coherent structure of the flow field. In contrast to pointwise actuation, acoustic flow control actuates the flow field globally by introducing small traveling wave perturbations at the speed of sound to the freestream.

Such an approach can simultaneously excite all the blades in a compressor/turbine stage, including regions that are difficult to target locally. However, the mechanism by which acoustic actuation reorganizes the flow field is not well understood. Global excitation means that the flow is simultaneously affected in multiple regions, and thus, the causal sequence of modification is significantly more complicated to untangle. The primary focus of this study is to identify the dominant underlying mechanism of acoustic flow control and investigate its potential application to simplified low-pressure turbine environments.

**1.1 Acoustic Flow Control.** The pioneering works on the use of acoustic actuation for flow control focused on enhancing the performance of airfoils [7–12]. Reference [11] showed that acoustic actuation can be used to achieve a delay in separation by enhancing the turbulent mixing of the near-wall region (for intermediate frequencies), as well as a reduction in the skin friction by suppressing the turbulence in the boundary layer (for very high frequencies) [11]. As a result, Ref. [13] found that acoustic excitations can provide a significant performance enhancement, increasing lift as high as 50% while decreasing drag by a similar amount. These examples reflect the effectiveness of the phenomena in cases

where primary loses are due to separation (the pressure drag), and/or where skin friction losses are predominant.

The key parameters of acoustic excitation are the amplitude and frequency of the wave, the optimal choice of which depends on the geometry of the body and the operating Reynolds number [14]. Since the severity of flow separation increases inversely with Reynolds numbers, small-scale engines or platforms operating at high altitudes are ideal targets for separation control.

The most suitable frequency for a given application is not yet well established and is an active area of research. Many studies, particularly in the 1980s, investigated the optimal acoustic frequencies for separation control [11,13–17] and found that a maximal flow response could be obtained by targeting frequencies associated with the inviscid instability of separated shear layers. Reference [16] showed that the optimal Strouhal numbers of acoustic excitation ($St = f_{opt}C/U_\infty$) scaled with the square root of Reynolds number ($Re = U_\infty C/\nu$), which is identical to the scaling of the Kelvin–Helmholtz (KH) mode. This optimal frequency choice led many investigators to conclude that acoustic waves directly excite the KH mode at the point of separation, and thereby modifying the separation dynamics. However, a number of alternative hypotheses persist about the physical mechanism by which the acoustic waves regularize the separating shear layer and reorganize the separation bubble dynamics.

**1.2 Physical Mechanisms of Acoustic Flow Control.** The proposed mechanisms for acoustic control can be divided into three main categories: direct control of the KH instability, indirect control of the KH instability via upstream wall modes, indirect feedback via the separation bubble itself.

Because separated flows are inviscidly unstable due to KH instability, many investigators proposed that the simplest explanation for acoustic control is direct actuation of the KH modes [2,16,18,19]. But this concept of direct interaction is challenging to establish experimentally due to the difficulty of creating shear layers without solid wall/splitter-plates/nozzles in their vicinity. Moreover, there are theoretical reasons to doubt whether planar (irrotational) acoustic waves can directly induce alterations in the spanwise vorticity in wall-free shear layers [20], without the viscous diffusive effects associated with the presence of a wall.

Due to these difficulties, an alternative hypothesis to the direct KH instability actuation emerged, in which the instability is assumed to be excited only indirectly through the development of wall modes in the attached flow, upstream of separation point. In studies of the leading edge of lifting bodies and flat plates, investigators have identified the presence of Tollmien–Schlichting (T-S) wall modes [21–23]. The leading edge was shown to be the location for transforming the long wavelength acoustic excitations into short wavelength T-S waves to which the flow is naturally receptive, where its wavelength $\lambda \propto x^{-1/2}$ decreases with the increasing distance $x$ from the leading edge. In a more recent work, Ref. [24] provided additional support for this alternative hypothesis in separating flows, by observing the presence of wall modes in the attached boundary layer region, upstream of the point of separation.

A final proposal for the mechanism of acoustic actuation is based on tonal noise generation in the vicinity of the airfoil trailing edge, which then propagates upstream via the potential feedback mechanism of the outer flow field, due to oscillations in the separated region. This upstream-oriented feedback would then excite T-S waves in the attached boundary layer, which would in turn organize the separating shear layer [24–26]. Therefore, the latter two mechanisms depend on indirect excitation of the shear layer via wall modes, but the key distinction is the direction of causality, whether the perturbation influences the flow in an upstream or downstream direction. The direct KH actuation also implies a downstream causality, at least from the separation point onward.

In order to achieve a detailed description of the physical mechanism of acoustic actuation, and in particular, to decide among the different competing hypotheses, we performed an experimental study along two axes. We first established the performance of an acoustic actuator acting on the flow over a hump, approximating the physics representative of high work and lift airfoils observed in modern turbine airfoils. The performance investigation was used to determine the acoustic parameters at which the greatest control effect could be obtained, and to characterize the scale of the performance enhancement. Moreover, the findings are contrasted with localized forms of control. Second, a follow-up study was conducted to allude on the flow physics and to analyze the precise mechanism by which the performance gains were achieved. Section 2 presents the experimental methodology for these two investigations, followed by the results in Sec. 3 in which we provide novel evidence in support of the wall mode hypothesis of acoustic actuation. Finally, in Sec. 4, we discuss the physical dynamics of the actuation mechanism and its implications on the design toward better acoustic flow control embodiments.

**1.3 Motivation.** Despite the extensive literature on acoustic flow control, there is no consensus on the mechanism of acoustic excitation impact on flow separation. Even in studies where acoustic excitation has been shown to primarily affect the attached boundary layer, a clear picture of the shape of the wall modes excited within the boundary layer (often presumed to be T-S modes) has not been demonstrated. One of the primary concerns of the present work has been to achieve adequate spatial resolution of the attached boundary layer to enable observation of wall modes. Careful observation of the near-wall flow can then be used toward answering the question of causality in acoustic actuation: Do the acoustic waves first influence the attached region and from there modify the separation behavior, or alternatively do the acoustic waves first reorganize the separation bubble downstream and from there modify the separation behavior upstream?

In addition to the fundamental, mechanistic questions, the application of acoustic flow control on the present geometry has significant practical engineering value. The airfoil geometry considered here is a simplified version of a high-work and high-lift low pressure turbine (LPT) blade, which is desirable for both high-altitude operations and micro gas turbine applications, but can suffer from significant flow separation challenges. Successful application of acoustic flow control in this geometry would therefore contribute to the reduction in the numbers of stages, blade count, and hence the overall weight required for a future engine prototype by as much as 15%. This would then translate to as much as a 10% increase in the range and endurance for a typical unmanned system.

## 2 Methodology

Flow separation control techniques, including both acoustic and hydrodynamic methods, have been successfully demonstrated in a wide range of simple flow configurations, thereby establishing a strong foundation for their use in both fixed wing aircrafts and rotating blades inside aircraft engines [10–12,15,27, 28]. Because this study is part of a larger effort to investigate the use of active flow control technologies in high-lift/high-work low-pressure turbine stages, the acoustic control will be applied to a reduced-order model of a turbine blade. We first discuss the design of the blade geometry, followed by a discussion of the wall-pressure and full-field velocity measurement techniques used on the final model subject to acoustic actuation.

**2.1 Reduced-Order Geometric Model.** A preliminary computational study was performed to assess the feasibility of applying acoustic flow control to complex turbine geometries. First, the primary goal was to design blade-like hump geometries for low-speed, wind tunnel, and water tunnel testing that are representative of high-speed turbine blades. A family of transonic turbines was designed to the same work and flow coefficients as the stage described in Ref. [29], albeit with different levels of the Zweifel

**Table 1  Pressure gradient characteristics of the LXFHW-LS airfoils**

| | L1FHW-LS | L2FHW-LS | L3FHW-LS |
|---|---|---|---|
| $M_{max}$ | inc. | inc. | inc. |
| $C_{p,max}$ | 1.42 | 1.61 | 2.05 |
| $\frac{s}{s_{total}}$ at $C_{p,\,max}$ | 0.261 | 0.307 | 0.225 |
| $\frac{s}{s_{total}}$ at $K_{relam}$ | N/A | 0.23 | 0.18 |
| $\frac{s}{s_{total}}$ at $K_{relam} - \frac{s}{s_{total}}$ at $C_{p,\,max}$ | N/A | −0.077 | −0.045 |
| $\frac{s}{s_{total}}$ at $K\,\mathrm{Re}_{\theta,sep}^2$ | 0.334 | 0.476 | 0.273 |
| $\frac{s}{s_{total}}$ at $K\,\mathrm{Re}_{\theta,sep}^2 - \frac{s}{s_{total}}$ at $C_{p,\,max}$ | 0.073 | 0.169 | 0.048 |

coefficient (Zw) in the blade row and with substantially higher design target efficiency. These turbine stages are referred to as LXFHW-*, where L is an LPT blade and X is a wildcard that denotes the meanline loading level of the blade (e.g., 1: Zw = 1.32, 2: Zw = 1.60, and 3: Zw = 1.78). Each front-loaded airfoil is a component of a high work stage. These blades have been designed in a variety of configurations (-*), and they can be used in both high-speed (HS) and low-speed (LS) linear cascades as well as rotating stages (T) and annular cascades (-A). An analysis similar to Ref. [30] is followed here to arrive at the current geometries, which are in line with the loading characteristics of LXFHW-LS blades. Furthermore, the current work also serves as an example of global flow management in low Reynolds number flows over a reduced-order geometry of heavily loaded LPT blades. The overall efficiency of any engine is increased as LPT performance improves, especially in micro gas turbine situations where flow separation is severe.

The low-speed humps studied in this experimental campaign were designed to match the loading characteristics over the same family of airfoils, and they represent a range of pressure gradients in the vicinity of peak suction that are consistent with those occurring on the blades themselves.

A quantitative comparison between the pressure variations over the low-speed humps and those over the LXFHW-LS airfoils near peak suction was made. The pressure gradient varied as the flow passes over the airfoil, moving from extremely favorable to strongly adverse. This is also true for the incompressible humps. Therefore, the pressure coefficient at peak suction ($C_{p,max}$) and fractional surface length ($s/s_{total}$) for the minimum pressure can be used to measure the closeness of the model humps to the blades. Additionally, one could measure the model quality via the fractional surface distance between the relaminarization point ($K_{relam}$, where $K_{relam} = (\nu/U^2)dU/ds = 3 \times 10^{-6}$) and the point of $C_{p,max}$. These two metrics are measures of the strength of the favorable pressure gradient. On the other hand, a measure of the strength of adverse pressure gradient is the fractional distance between locations corresponding to $C_{P,max}$ and where the Thwaites pressure gradient parameter is −0.09 (a value typically associated with separation, $\lambda\theta = K\mathrm{Re}_\theta^2 = -0.09$). All of these values are tabulated in Tables 1 and 2, for both the LXFHW-LS airfoils and the low-speed humps. They were estimated by two-equation Reynolds-averaged Navier–Stokes (RANS), analysis of each geometry. The tables establish the consistency of the pressure distributions in the incompressible ("inc." in the tables) humps with LXFHW-LS airfoils. Hence, the low-speed humps appear to be a suitable, simplified geometry to study the applicability of flow control on high-lift, high-work low-pressure turbine blades [31].

It is expected that the application of flow control to an LPT blade is advantageous for operation at high-altitude conditions or for very small-scale machines where the Reynolds number is low. For a high-lift, high-work LPT airfoil, the geometric location of separation onset may not vary appreciably as the Reynolds number decreases on account of the severity of the adverse pressure gradients on the blade suction side. However, this means that the local momentum-thickness Reynolds number in the vicinity of separation can vary considerably. For the LXFHW series of airfoils, momentum-thickness Reynolds number near separation onset varied by an order of magnitude (e.g., 50–500) over the operating conditions of the airfoils, and the application of flow control is of the greatest interest at the lower end of that range.

The assumption underlying the analysis of the hump models is that evidence for effective flow control on low-speed humps provides preliminary support for implementing similar technologies at the higher level of complexity (such as low-speed linear cascades, and eventually at high-speed cascades and rotating rigs). The hump profiles considered in this study are shown in Fig. 1. The profiles were imported into SOLIDWORKS and extruded to create a 3D hump of 20 cm span, with trenches at 3 cm from each side to avoid corner vortices. The resulting models were 3D printed (Original Prusa i3 MK3S) from PLA and PETG plastic and sanded to achieve a surface roughness of about 12 $\mu$m. The models were then used for both surface pressure and full-field velocity measurements.

**Table 2  Pressure gradient characteristics of the low-speed humps**

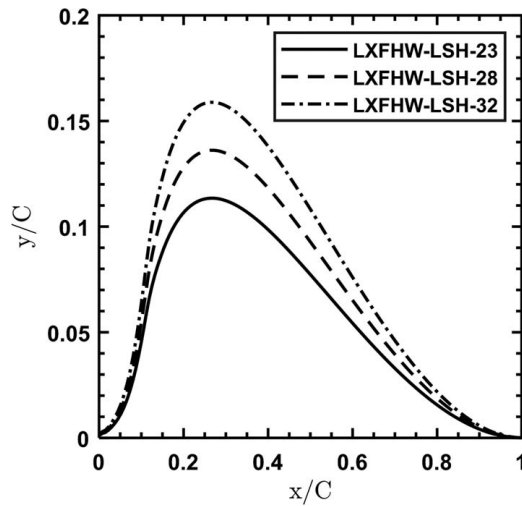| | LXFHW-LSH-23 | LXFHW-LSH-28 | LXFHW-LSH-32 |
|---|---|---|---|
| $M_{max}$ | inc. | inc. | inc. |
| $C_{p,max}$ | 2.15 | 2.30 | 2.49 |
| $\frac{s}{s_{total}}$ at $C_{p,\,max}$ | 0.237 | 0.246 | 0.264 |
| $\frac{s}{s_{total}}$ at $K_{relam}$ | 0.186 | 0.2 | 0.211 |
| $\frac{s}{s_{total}}$ at $K_{relam} - \frac{s}{s_{total}}$ at $C_{p,\,max}$ | −0.051 | −0.046 | −0.053 |
| $\frac{s}{s_{total}}$ at $K\,\mathrm{Re}_{\theta,sep}^2$ | 0.307 | 0.314 | 0.311 |
| $\frac{s}{s_{total}}$ at $K\,\mathrm{Re}_{\theta,sep}^2 - \frac{s}{s_{total}}$ at $C_{p,\,max}$ | 0.07 | 0.068 | 0.047 |

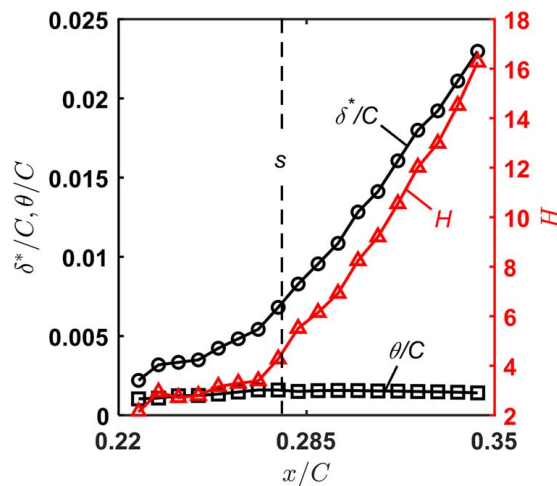**Fig. 1 Hump geometries derived from the high-work and high-lift turbine blades (LXFHW-LS)**



**Fig. 2 Integral boundary parameters (displacement thickness ($\delta^*/C$), momentum thickness ($\theta/C$), and shape factor ($H$)) in the neighborhood of the point of separation denoted by the vertical line "s." The Reynolds number, here, is 46,500.**

In addition to the hump surface pressure and relaminarization parameters, we also measured the integral boundary layer parameters, specifically the displacement ($\delta^*$) and momentum thicknesses ($\theta$), along with their ratio the shape factor ($H$) for the LXFHW-LSH-28 hump that will be the primary geometry for the experimental campaign. Figure 2 shows a typical streamwise variation of $\delta^*$, $\theta$, and $H$ in the neighborhood of the separation point (shown as the vertical line "S" in the figure), measured using particle image velocimetry (PIV) for a Reynolds number of 46,500. Since the variation of $\theta$ is not appreciable, it is often used as the local length scale in separated flow literature [32–35], as discussed in detail in the next section.

**2.2 Static Pressure Measurements in Wind Tunnel.** The experiments for static pressure measurements were designed to obtain the pressure coefficient across the chord of the hump and to determine the relative change in the lift coefficient between actuated and unexcited flow fields. The pressure measurements were performed in a low-speed (<50 m/s) open-loop wind tunnel shown in Fig. 3. A centrifugal blower, acoustically isolated from the test section, drives the suction flow in the tunnel, and a settling
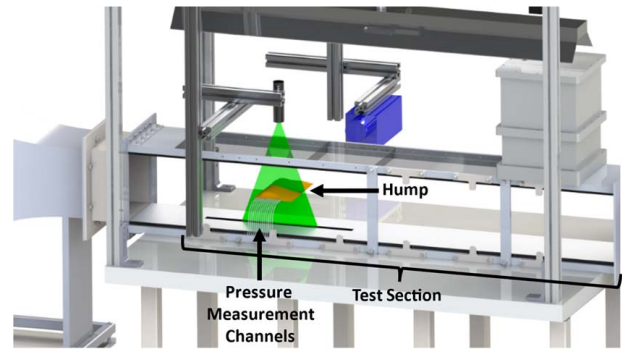


**Fig. 3 The wind tunnel facility**

chamber, placed upstream of the blower, dampens out pressure fluctuations. The test section is 1.5 m long and the inlet assembly is attached to the test section via a 12 cm long connection piece containing a taut steel wire fine mesh (25 $\mu$m cell size) used to introduce a realistic level of freestream turbulence, in the order of 6%. The cross-sectional area of the tunnel is $0.2 \times 0.2$ m$^2$. Additional details about the wind tunnel are available in Ref. [28]. The Reynolds number range of the flow was 28,000–47,000, based on chord and the freestream velocity. The static pressure on the surface of the humps is measured differentially with respect to the atmospheric conditions. Each hump was manufactured with 13 holes of 2 mm in diameter at the interior serpentines of the geometry, while the opening on the geometry surface was limited to 0.5 mm. Each pressure tapping was oriented such that its opening would be perpendicular to the surface profile. The pressure measurements were performed using Scanivalve Model DSA 3217 transducer with maximum differential pressure of 2490 Pa at an accuracy of $\pm10$ Pa. Static pressure data were acquired at a sampling rate of 10 Hz over a measurement duration of 50 s. Therefore, the reported static pressure is an average of 500 samples. The 95% confidence interval (for a standard normal distribution of the error [36]) of the measured differential pressure about the sample mean is $\pm0.5$%. Following Ref. [37], the uncertainty in coefficient of pressure $C_p$ translates to $\pm1.0$%. For coefficient of lift $C_L$, the 95% confidence interval (for a standard normal distribution of the error) is $\pm2$%. The spatial resolution of the pressure distribution is 0.11C. The fact that the geometry mimics highly front-loaded LPT blades (LXFHX-LS), coupled with the fact that viscous effects are significant, results in an expectation of early separation, which is ideal for studying the separation control capacity of acoustic actuation.

The acoustic excitations were generated by a loudspeaker (Mackie DLM-8; 65 Hz—20 kHz, maximum SPL 140 dB) that was placed in a sealed casing on the top wall, downstream of the test section. To enable the permeation of the acoustic pulsations in the test section, a fine steel wire membrane with 25 $\mu$m cell size was placed between the speaker cavity and the channel test section. Purely sinusoidal input voltage signals are provided to the loudspeaker by a Tektronic AFG 3021C function generator.

The wind tunnel testing was done over humps with various peak suction pressures and associated diffusion ratios (LXFHW-LSH-23, LXFHW-LSH-28, and LXFHW-LSH-32). The effect of frequency and amplitude of acoustic excitation was investigated for each geometry over a range of free-field velocities. In the detailed boundary layer PIV investigations, LXFHW-LSH-28 is focused upon as a representative geometry.

**2.3 Velocity Field Measurements in Water Tunnel.** In order to describe the physical acoustic actuation mechanism, high fidelity spatio-temporal velocity field measurements were needed to resolve the near-wall region. Therefore, the second phase of the experiments was conducted in a water tunnel facility at matched Reynolds

number of 46,500 on the reference hump (LXFHW-LSH-28) shown in Fig. 4. The water tunnel cross section was $0.2 \times 0.2$ m$^2$ with test section length 2 m. The turbulence intensity at the inlet of the test section was measured to be 0.5%. The hump was placed at 1 m downstream of the inlet contraction. An underwater speaker (DNH Aqua-30; with frequency range of 20 Hz—20 kHz, and maximum SPL of 118 dB in water) was used for the acoustic excitation. The KH frequency of 30 Hz was first identified from the spectral analysis of the separating shear layer of the unactuated flow, as shown in Fig. 5, and therefore, the flow control was performed at this frequency. The $St/\sqrt{Re}$ axis shown in Fig. 5 is the relevant, nondimensional frequency as discussed in detail in Sec. 3.1.

As in the wind tunnel testing, the speaker was placed at the downstream end of the test section (1 m or 9C downstream of the hump) to avoid distorting the incoming velocity field. The soundwaves travelled upstream, against the streamwise velocity direction to minimize the advective effects of the freestream flow on acoustic disturbances. Similar configurations are found in the studies of Refs. [13,14,16]. The speaker was driven by an amplifier (Yamaha XMV4140), and the sinusoidal input signals were generated and delivered by a function generator (Tektronic AFG 3021C).

Time-resolved, 2D planar PIV measurements were performed in the streamwise/wall-normal region above the hump using a dual-pulse laser (Litron LD30–527) and high-speed CMOS camera (Phantom Veo 440L, $2560 \times 1600$ px). Glass spheres with a size of 10 $\mu$m were used as tracer particles. Double frame recording was utilized with the $\Delta t$ range of 150–300 $\mu$s. The resolution of the images (50–100 px/mm) was changed according to the region of interest, resulting in a range of 4800–20,000 frames for each measurement for 5 s of acquisition. The resulting image pairs were processed by commercial PIV software (LAVISION DAVIS 10.1), using a four-pass cross-correlation method, with initial and final window sizes of $128 \times 128$ px and $24 \times 24$ px, respectively, and a constant overlap of 75%. The acquisition frequency is chosen as 1500 Hz for the unexcited flow and as 900 Hz for the excited conditions (corresponding to 30 times the supplied acoustic excitation frequency). These velocity fields were phase averaged to provide 30 fields separated by 12 deg, resulting from an average of 160 fields each.

The PIV uncertainty was assessed by the correlation statistics quantification method [38]. The method takes two consecutive frames, and warps one on top of the other using the displacement field. Then, the two frames are analyzed with the discrete window offset technique. In our analysis, we used a $24 \times 24$ px window size with Gaussian weight. The uncertainties in the mean and the fluctuating PIV velocity measurements were evaluated following the formulation of Ref. [39]. The 95% confidence interval
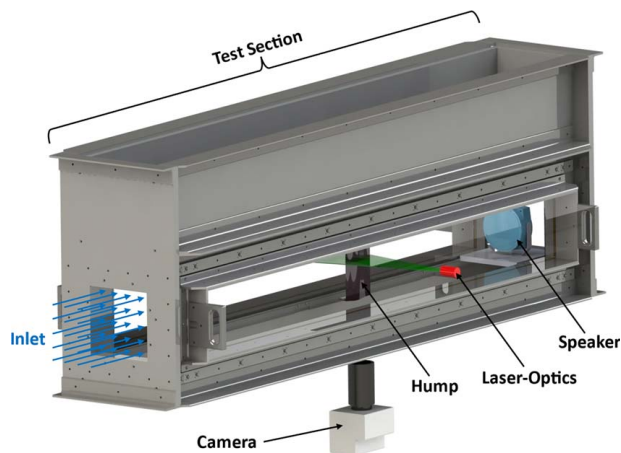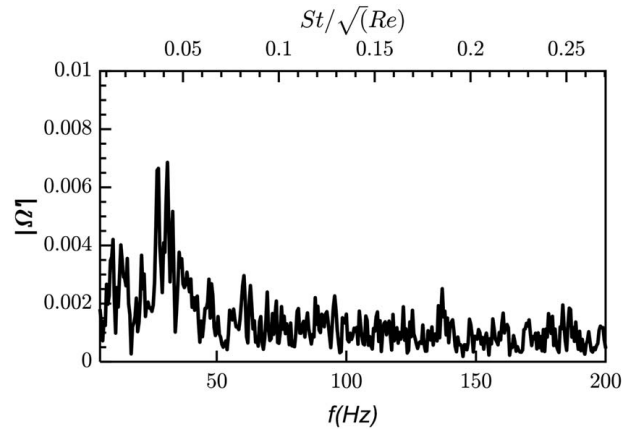


**Fig. 5 Spectrum of nondimensional fluctuating vorticity in the unactuated shear layer at $X = 0.36C$ and $Y = 0.16C$**

(assuming normalized Gaussian distribution for the error, regardless of the distribution of the variable under consideration [36]) for velocity is $\pm 1\%$ and for vorticity is $\pm 2\%$ of the mean. The total number of temporal fields involved in the statistics was 4852.

## 3 Results

**3.1 Enhancement of Lift Coefficient Through Acoustic Excitation.** The acoustic actuation exerts a strong influence on the separation behavior of the flow over the hump, resulting in a significant change to the distribution of surface static pressures. Over the nominal pressure gradient hump (LXFHW-LSH-28), Fig. 6 shows the comparison of static pressure coefficient, $C_p = (P - P_\infty)/(P_o - P_\infty)$, for the computed potential solution distribution, the tested unexcited conditions, and excited case at 200 Hz. The potential flow solution was obtained by using inviscid flow solver in ANSYS FLUENT. The departure from the inviscid distribution is considerable, which indicates a strong separation in the unexcited case. When actuated, the peak suction pressure is augmented considerably, reflected in the pressure recovery of attached flow further downstream.

The net effect of the actuation on the overall pressure distribution can be quantified by integrating the pressure coefficient across the suction surface, resulting in the lift coefficient, $C_L$, defined as follows:
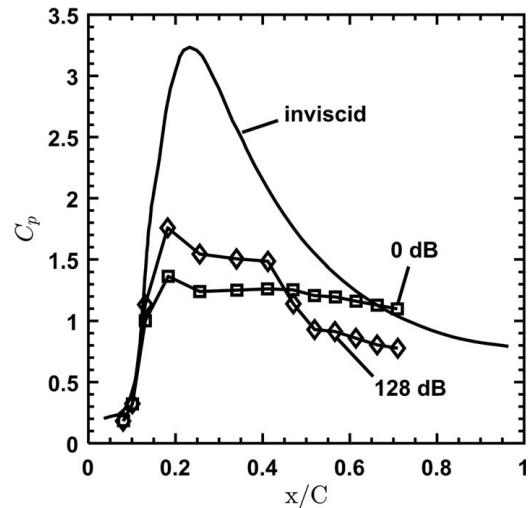


**Fig. 4: The water tunnel facility**



**Fig. 6 $C_p$ comparison of unexcited (0 dB) and acoustically excited (128 dB) cases with inviscid solution for hump (LXFHW-LSH-28), Re = 42,700, $F$ = 200 HZ**
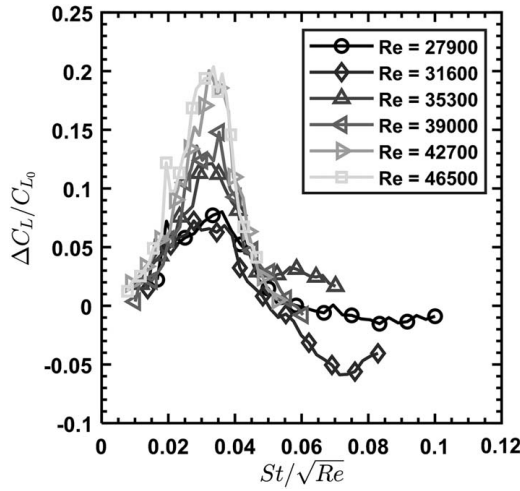
**Fig. 7  Scaling of the optimal Strouhal number with Reynolds number for hump (LXFHW-LSH-28) with excitation amplitude, 128 dB**



**Fig. 8  Lift enhancement as a function of excitation amplitude for hump (LXFHW-LSH-28), Re = 42,700, $f$ = 200 Hz (St/$\sqrt{\text{Re}}$ = 0.02)**

$$C_L = \int_{x_1}^{x_2} C_p \, d(x/C)$$

To quantify the relative improvement of the lift coefficient under actuation, we defined $\Delta C_L/C_{L0}$ to represent the relative change in the lift coefficient with respect to the unactuated flow.

Figure 7 presents the lift enhancement observed on the same hump geometry noted earlier, over a range of flow velocities and excitation frequencies at an excitation amplitude of 128 dB. The data are nondimensionalized with St/$\sqrt{\text{Re}}$, and the reasonable collapse indicates that the selected scaling is appropriate. In their seminal work, Ref. [16] showed that the optimal Strouhal number scales with the $\sqrt{\text{Re}}$. At the time, however, they were not aware of the origins of this scaling. It was later shown that $\text{St}_{\text{opt}} \sim \sqrt{\text{Re}}$ can be derived (discussed subsequently) from the inviscid KH instability frequency of mixing layers [10,19]. In this experiment, the optimal forcing response was observed around St/$\sqrt{\text{Re}} \sim 0.035$, where the lift enhancement increased from 5–20% with Reynolds numbers.

The Reynolds number dependence can be incorporated into the definition of a new "local" Strouhal number, $\text{St}_{s,\theta} = (f_{\text{opt}} \, \theta_s)/U_s$, by utilizing the momentum thickness at the separation point $\theta_s$ as the relevant length scale, instead of the chord length, where asymptotically, $\theta_s/C \sim 1/(\text{Re}^{1/2})$, and the local freestream velocity, $U_s$. The variation of the integral parameters along with shape factor is shown in the vicinity of the point of separation (depicted by the vertical line "S") in Fig. 2. It is interesting to note that momentum thickness is almost a constant in the neighborhood of separation; this is an important characteristic of pressure gradient-induced flow separation [32–35]. It has been, therefore, a preferred local length scale. The KH frequency has been shown to scale as follows: $(f_{\text{KH}}\theta_s)/U_s \approx 0.012$ [16,40], which is nearly identical to the optimal forcing Strouhal number expressed in a local form, $\text{St}_{\text{opt},\theta} = (f_{\text{opt}} \, \theta_s)/U_s = 0.013$ calculated from Fig. 7. This clearly indicates that KH mode is excited by the actuation either directly or indirectly, where the precise mechanism of the excitation is discussed in Sec. 3.3.3. A drawback of this local scaling is that the velocity profile at the separation point must be known to estimate $\theta$.

The lift enhancement by acoustic flow control is a function of the amplitude of excitation. Therefore, lift enhancement was measured over a range of excitation amplitudes for a representative frequency of 200 Hz (St/$\sqrt{\text{Re}}$ = 0.02) as shown in Fig. 8. (The choice of any frequency around the broad optimal peak of St/$\sqrt{\text{Re}}$ = 0.035 (in Fig. 7) does not change this overall trend of lift enhancement with excitation amplitude.) The findings indicated that $\Delta C_L/C_{L0}$
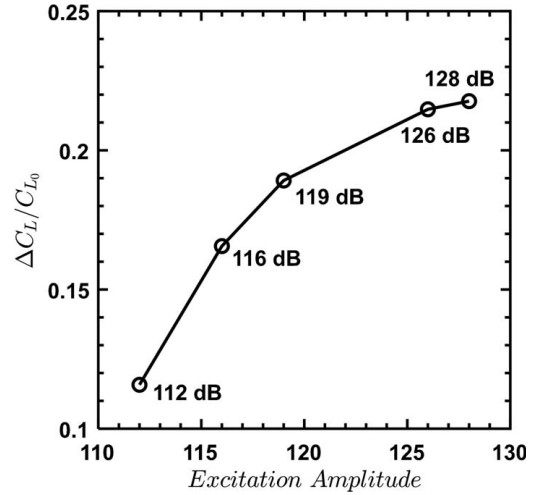
increases with the excitation amplitude but appears to reach an asymptotic limit at higher SPL values.

Finally, humps of several diffusion ratios (maximum thicknesses) were considered to characterize the effect of the change in geometry to the lift enhancement. The different geometries considered were LXFHW-LSH-23, LXFHW-LSH-28, and LXFHW-LSH-32 (wherein the suffix number of each of the geometries denotes twice its percentage maximum thickness). For a given excitation frequency and amplitude ($f$ = 200 Hz, 128 dB for Re = 42,700, St/$\sqrt{\text{Re}}$ = 0.02), it was observed that $\Delta C_L/C_{L0}$ increases from 0.01 to 0.2 to 0.36 with the increase in diffusion ratio of the humps from LXFHW-LSH-23 to LXFHW-LSH-28 to LXFHW-LSH-32.

**3.2  Efficiency Comparison.** A relative effectiveness metric for flow actuation was defined as the ratio of the relative increase in lift coefficient, $\Delta C_L/C_{L0}$, with respect to the momentum coefficient $C_\mu$ in order to evaluate the effectiveness of acoustic control compared to different control strategies in the literature. The momentum coefficient has traditionally been defined by Refs. [2,41] as representing the momentum flux generated by flow actuation, calculated through a spanwise/wall-normal plane of height $H$, against the freestream momentum flux calculated with planform area $A_{\text{ref}} = C \times S$ (where $C$ and $S$ are the chord and span of the blade).

$$C_\mu = \frac{\dot{m}U_j}{0.5\rho U_\infty^2 A_{\text{ref}}} = 2\left(\frac{H}{C}\right)\left(\frac{U_j}{U_\infty}\right)^2$$

For a localized actuator (like a suction/blowing-jet through a slot), the spanwise/wall-normal plane of actuation is easily defined by the slot height, $H$, multiplied by the span. However, in a global actuator (like acoustic actuation), the actuation plane theoretically extends to infinity, but the intended actuation is focused only on the boundary layer thickness, $\delta$, itself. Therefore, the lower-bound on the actuation plane height for acoustic actuation should scale with the boundary layer thickness, and an upper bound on actuation plane height (which represents the global actuation effort) should scale with the largest length scale in the system, i.e., the chord length of the airfoil. By defining two momentum coefficients corresponding to these two length scales, we can provide physically meaningful bounds on the momentum flux for acoustic actuation for energetic comparison with local actuation techniques.

The relative enhancement of lift $\Delta C_L/C_{L0}$ versus $C_\mu$ is plotted in Fig. 9. Additionally, local actuation techniques from the literature
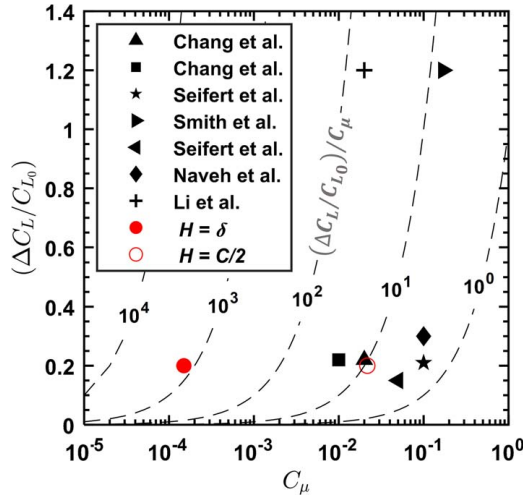
**Fig. 9 Relative effectiveness comparison between acoustic flow control and other active flow control techniques. The lift enhancement with respect to momentum coefficient ($C_\mu$) [3,4,42–45].**



**Fig. 10 Unexcited (top) and excited (bottom) mean non-dimensional vorticity fields, $U_\infty = 0.4$ m/s, $F = 30$ Hz**

are shown in black markers. The local ($H = \delta$) and global ($H = C/2$) estimates of $C_\mu$ for present measurements are shown as a solid and empty red circle, respectively. The dotted lines are iso-lines of the relative effectiveness parameter, defined as the ratio of the output lift enhancement and input momentum flux (($\Delta C_L/C_{L_0})/C_\mu$). Studies presented in Fig. 9 with higher values of this parameter appear to the left and have comparatively higher actuation effectiveness. The relative effectiveness for the acoustic actuation in the local sense is, at least, an order of magnitude higher than the rest. This advantage points to the enhanced efficacy of the strategy in terms of the overall flow dynamics and its physics. Heuristically, it could be thought as a much cleaner control strategy among others due to the fact that viscous losses in an acoustically actuated flow are much smaller in comparison to other strategies.

On the other hand, since the acoustic actuation is ultimately global in nature, most of the acoustic energy, for example, the acoustic energy in most of the freestream, is wasted. This is reflected in Fig. 9 by the global $C_\mu$ (by the empty red circle), wherein its relative effectiveness is lesser than its local counterpart, but comparable to others (and better than some). It should, however, be noted that the relative effectiveness of acoustic control (global) is a function of the $H/C$—pitch-to-chord ratio (the solidity)—when applied to an acoustic control, but for the other strategies, it is practically independent of the number of blades. The "cleaner" feature of acoustic flow control makes it an intriguing candidate to delve into its mechanistic aspects.

**3.3 Modification of Flow Dynamics.** The significant effect of acoustic excitation on the lift enhancement of airfoils for relatively small energetic costs compared to localized actuation systems raises the question of the mechanics of the acoustic excitation: How does the acoustic perturbation reorganize the separation bubble in such a substantial way? In order to answer this question, a second series of experiments were performed in a water tunnel facility, utilizing the same geometry as the aforementioned experiments, but with high-resolution, time-resolved velocity field measurements using PIV. These velocity field measurements and their accompanying analysis allow for a careful examination of the fluid mechanics of acoustic flow control.

*3.3.1 Mean Vorticity Field.* The mean vorticity fields for the unactuated and actuated flow fields over the hump are shown in Fig. 10. The vorticity is nondimensionalized by $U_\infty/\theta_s$. In the unactuated flow, the negative vorticity of the shear layer peels away from
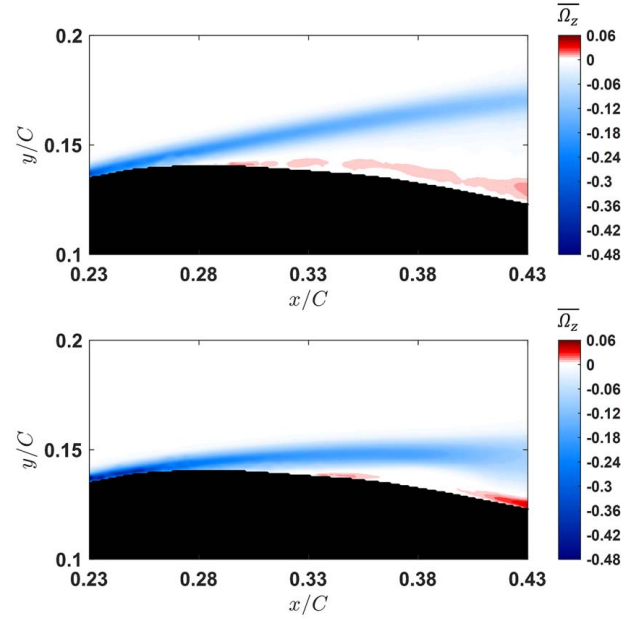
the body with a high angle, resulting in a large separation bubble characterized by positive vorticity near the wall. At Re = 46,000, with actuation at $f = 30$ Hz (St = 8.7, St/$\sqrt{\text{Re}} \sim 0.04$) and amplitude of 190 dB (equivalent to 128 dB in air), the shear layer peels off at a significantly shallower angle, and from a separation point that shifts noticeably downstream. This shift is consistent with the static pressure measurements, although no appreciable change in pressure is seen at the specific location of separation observed from the PIV, because the pressure resolution is 0.11C and the shift in the separation point is only 0.04C. The resulting separation bubble is substantially diminished in size. These mean field results illustrate the physical flow dynamics associated with the pressure coefficient measurements reported earlier. However, the mean field is unable to reveal the dynamics of the acoustic perturbation, in particular how it organizes the flow field. Thus, the instantaneous measurements were phase averaged in sync with the acoustic excitation itself.

*3.3.2 Phase-Averaged Vorticity Fields.* The fluctuating vorticity fields were phase averaged with respect to the acoustic actuation in order to identify coherent modes within the actuated flow. The fluctuating vorticity field is denoted $\Omega'_z(x, y, j)$, where $j$ is the $j^{\text{th}}$ planar slice in the time series, with $N$ being the total number of temporal slices. The frequency of the acoustic excitation was $f_{\text{ex}} = 30$ Hz. The sampling frequency of acquisition was $f_s = 900$ Hz. The integer $k = f_s/f_{\text{ex}} = 30$ is the number of phases in one cycle of actuation. $\Omega'_z(x, y, j)$, therefore, was phase-averaged $\overline{\Omega'_z}$ as follows:

$$\Omega'_{z,m}(x, y) = \frac{\sum_{n=1}^{\frac{N}{k}} \Omega'_z(x, y, k(n-1) + m)}{N/k}$$

where $m$ is an integer ($1 \leq m \leq k$) representing the phase index. The same phase-averaging procedure was also performed for velocity. The 95% confidence interval (for a standard normal distribution of the error, with 161 temporal fields in each phase) for the phase-averaged velocity and vorticity was estimated to be ±3% and ±5%, respectively. The phase-averaging process is shown schematically in Fig. 11. The resulting, phase-averaged vorticity fields are shown in Fig. 12 for both the actuated and unactuated cases at a single phase. In the Appendix, six different phases of the actuated case are presented.
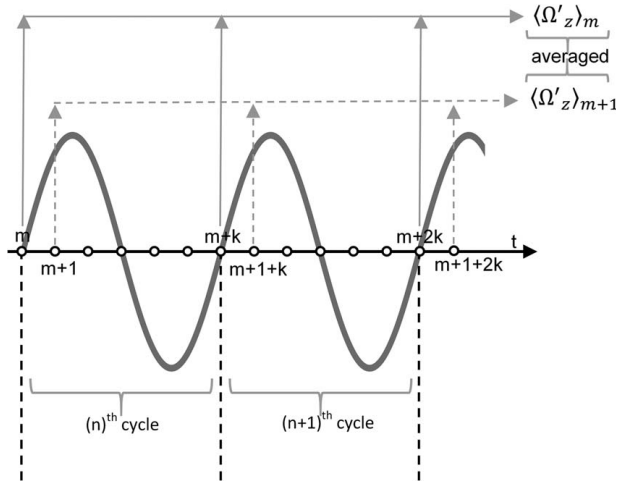
**Fig. 11 The procedure for phase averaging on the basis of imposed fluctuations. Thirty velocity/vorticity fields were acquired in one cycle of imposed oscillations. Phase-averaged fields were obtained by averaging fields corresponding to same phase values, I.E., I, I + 30, I + 60,..... and so on.**

The unactuated phase average can be considered as an instantaneous vorticity field that has been filtered to only include oscillations at the actuation frequency, and it shows the natural vortex oscillations in the flow at that frequency when there is no external stimulation. For the unactuated case, we observe a large field of randomly oriented, small-scale vortical structures associated with the break-up of the shear layer downstream of the separation. In the upstream where there is attached flow, the near-wall filtered vorticity also appears largely random across the height of the boundary layer (see Fig. 12).

In the actuated flow, the phase-averaged fluctuating vorticity in the attached region exhibits clear two-layer stratification, representing the spatial structure of the very-long wavelength acoustic modes. The organization of the vorticity in this upstream region is less apparent in the immediate vicinity of the separation point but appears to re-emerge in the structure of the separated shear layer, which is composed of large-scale coherent pairs of vortices, corresponding to the two layers of the upstream wall modes. The large-scale vorticity organization also appears inside the separation bubble and also towards the wall. The latter is perhaps induced as secondary vorticity from the large-scale vortices advecting away from the surface.

Qualitatively, it appears that the upstream wall modes correspond to the eventual organization of the shear layer downstream. Therefore, we examined the phase-averaged vorticity profiles of these modes, shown in Fig. 13. The profiles of the wall modes upstream of the separation point are consistent with the classic Stokes' layer type of modes predicted by the linear stability analysis, of which Tollmien–Schlichting modes are the most unstable [12]. The modes develop due to the interaction between the periodic pressure forcing of the flow and the viscous influence of the wall, resulting in a two lobed structure of alternating-sign vorticity. In the streamwise velocity sense, this represents interchanging gradients, resulting in two regions of near-wall alternating shear. The presence of these well-defined modes suggests that the organization of the shear layer may begin far upstream, and not at the point of separation itself. But phase-averaged analysis alone cannot resolve the causal relationships between the upstream wall modes, the separation point, and the separation bubble. Therefore, we employed a spatio-temporal correlation analysis to dissect the interconnections between these flow regions.

*3.3.3 Identifying Causality Through Correlation Analysis.* A number of mechanisms have been proposed for explaining the influence of acoustic forcing on the separation process. Two of the proposals entail opposite causes for the ultimate reduction in the separated flow region and change in the separating streamline angle. In the first approach, the acoustic forcing results in direct modification of the separation bubble itself, which then regulates the separation point upstream of the bubble. In the second approach, acoustic forcing reorganizes the attached flow upstream of the separation point via near-wall oscillatory modes, which then regulate the separation point downstream. The first approach suggests that the regularizing effect of the forcing would be felt first in the separation bubble region, and only later in the upstream, while the second approach suggests the opposite — that the regularizing effect would be experienced first in the development of wall modes, prior to any change in the separation bubble. The transient behavior of the system, immediately before and after acoustic actuation is initiated, can therefore be used to examine these two causal directions, by measuring how the transient response of the flow varies spatially: Does the separation bubble transient precede the upstream wall mode transients, or is the reverse the case?

To determine the causal direction of acoustic influence, a set of transient experiments were performed in which the actuator was initiated at the midpoint of the duration of a time-resolved PIV measurement. Examination of the instantaneous velocity signals showed an abrupt influence of the actuation at the time of excitation, followed by a long transient that extended over roughly 15 periods of excitation (depending on location), over which the separation bubble and outer flow adjusted to the external forcing. However, visual inspection of the velocity time series at different spatial locations was inconclusive in determining whether the excitation emerged in one region before another. Therefore, a time-correlation approach was employed to determine the lag between spatially varying points in the flow field.

The correlation analysis utilized a single reference location ($y = 0.3\delta$) taken in the neighborhood of the pre-excitation separation point, since it is a natural divider between upstream and downstream regions. All other points were then correlated against this spot. However, the results of the correlation analysis were robust to the precise choice of reference location to within $1.5\delta$ in the streamwise and $0.25\delta$ in the wall-normal directions where $\delta$ is the boundary layer thickness at the streamwise location of the reference. Normalized cross-correlations were performed between the reference and test locations over time series, which extended for the length of the transient (15 cycles), according to the following equation:

$$R(\Delta t) = \text{ref}(t + \Delta t)\, \text{test}(t)$$

The range of temporal lags between these time series was confined to plus or minus half a period of the actuation ($\pm \pi$), in order to identify the dominant phase lag between the reference and test signals.

The correlation process is illustrated in Fig. 14 for a downstream test location relative to the separation reference point. If the transient behavior in the test location is delayed relative to the reference (i.e., it occurs later in time), then the temporal correlation should indicate a negative phase lag, $\Delta t < 0$. If the behavior in the test location precedes the reference, then $\Delta t > 0$.

For the time period prior to the actuation, Fig. 15 (top subfigure) maps the temporal delays for all test locations across the flow field with respect to the reference location near the separation point. Upstream, we find, $\Delta t < 0$, indicating that unsteadiness at the separation points occurs before the upstream fluctuations. Downstream, we find that $\Delta t > 0$, indicating that the unsteadiness at the separation points occurs after the downstream fluctuations. This means that the natural oscillations of the separation bubble modify the outer flow field, which then causes changes to the upstream. In other words, the change from $\Delta t < 0$ to $\Delta t > 0$ in the streamwise direction indicates signaling in the upstream direction, through potential interactions. The observation is consistent with the tonal noise feedback mechanism [24,26,46].
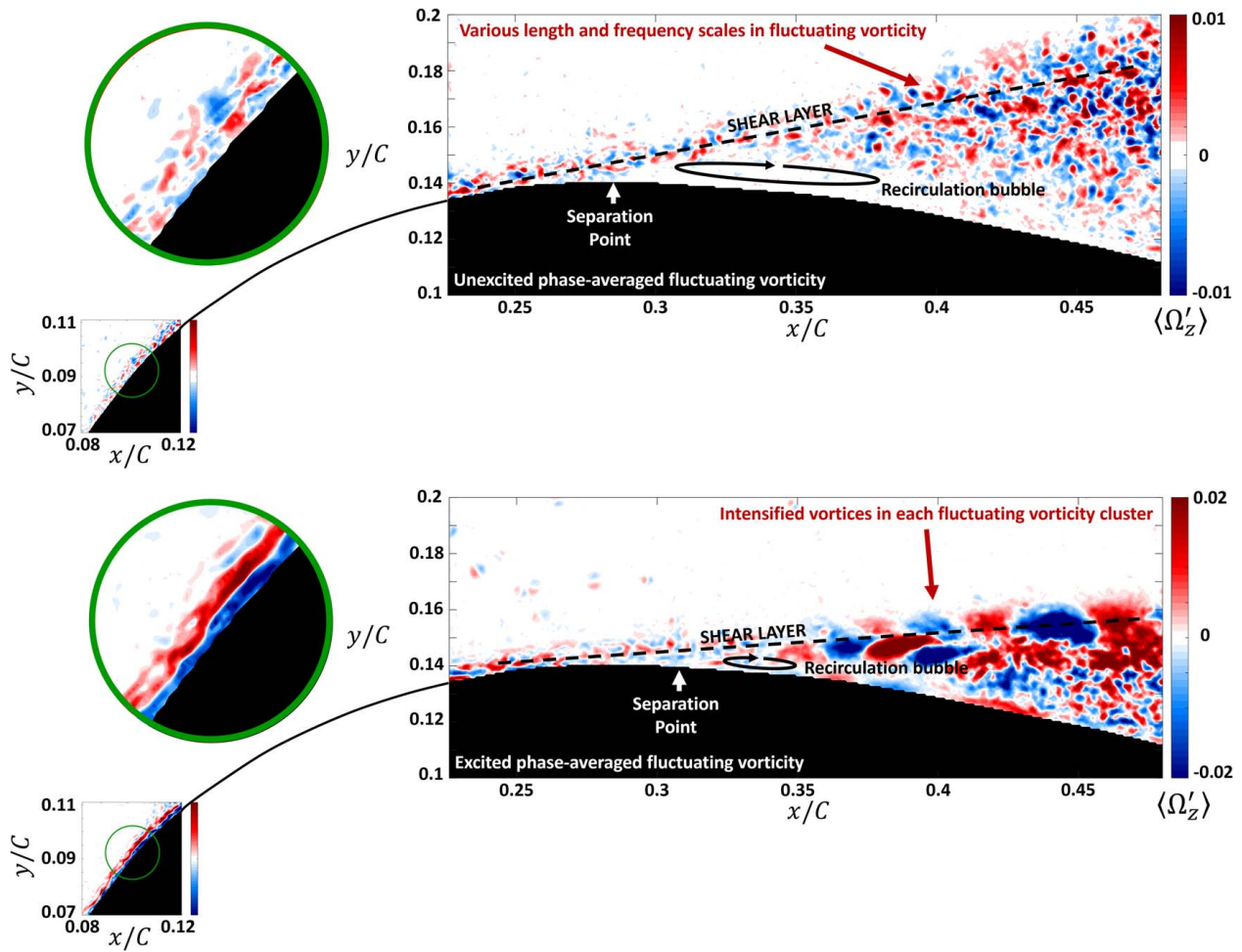
**Fig. 12 Unexcited (top) and excited (bottom), phase-averaged fluctuating nondimensional vorticity fields comparison in the upstream (attached, left) and downstream (separating, right) regions, $U_\infty = 0.4$ m/s, $F = 30$ Hz. Insets show zoomed in view of the attached region.**

For the period of the transient starting immediately after the initiation of the acoustic excitation, Fig. 15 (bottom subfigure) maps the same type of temporal delays. Here, we observe that the time lag trends are reversed. Now, the time delay upstream
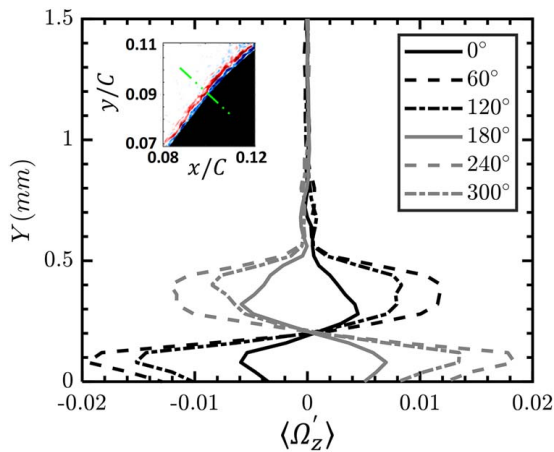


**Fig. 13 Phase-averaged nondimensional vorticity profiles in the attached region of the hump ($X/C \sim 0.1$, indicated by a wall-normal dashed line in the inset) at different phases of a shedding cycle, $U_\infty = 0.4$ m/s, $f = 30$ Hz**
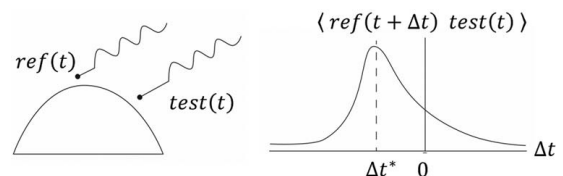
of the separation point is $\Delta t > 0$, indicating that the flow unsteadiness occurs first in the wall modes of the attached flow and then propagate down to the attachment point. And downstream of the separation point, $\Delta t < 0$, indicating that the unsteadiness at the separation point precedes the changes to the recirculation region. In this case, the unsteadiness proceeds in the streamwise direction, from the attached flow toward the separated flow.

The temporal lag analysis suggests that change in the separation bubble is driven by the upstream wall modes that develop due to the actuation. These wall modes then advect downstream and regularize the shear layer at the point of separation, resulting in the subsequent modification of the separation bubble. The calculated time lags are not consistent with the hypothesis that the bubble itself drives the separation changes and upstream wall modes. Nor are they consistent with the hypothesis that the separation
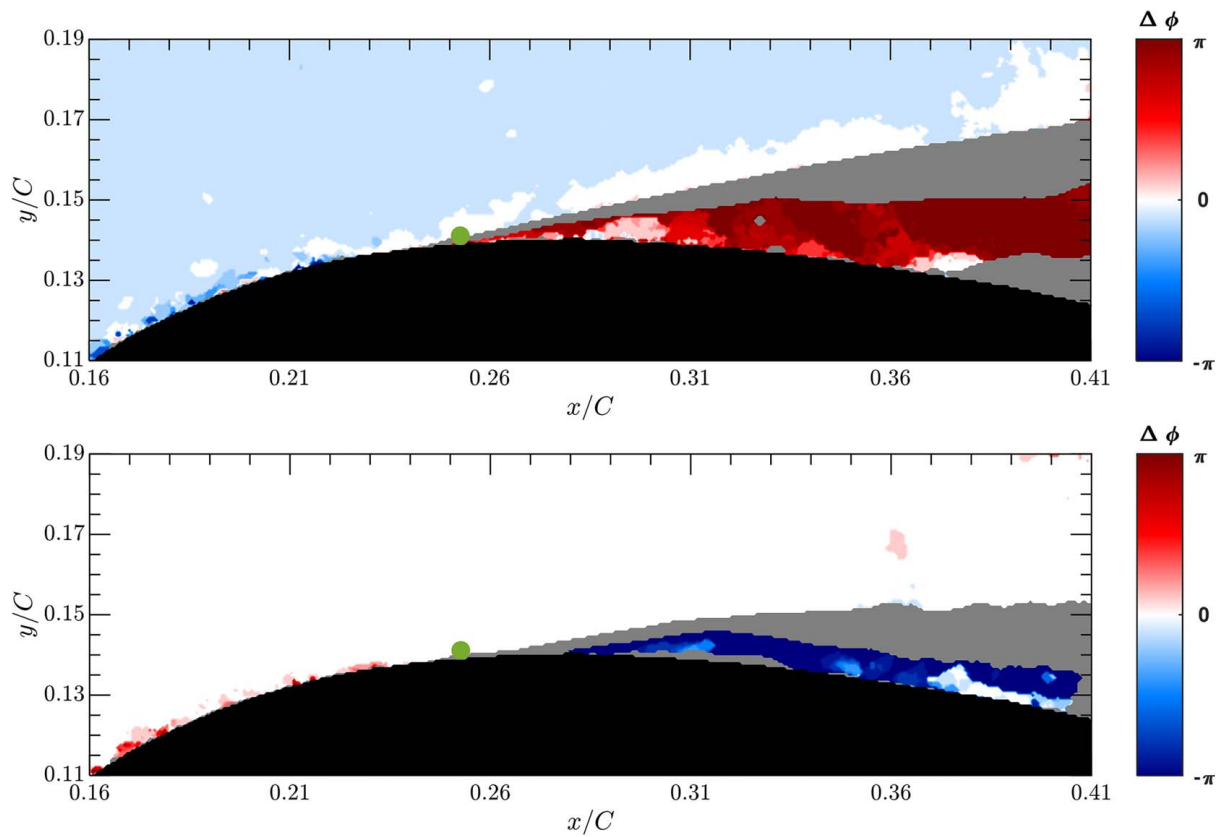


**Fig. 14 Explanation of cross-correlation**

**Fig. 15  Lag distribution around the flow field based on cross-correlation. Shift in flow of events between unexcited (top) and excited (bottom) flows.**
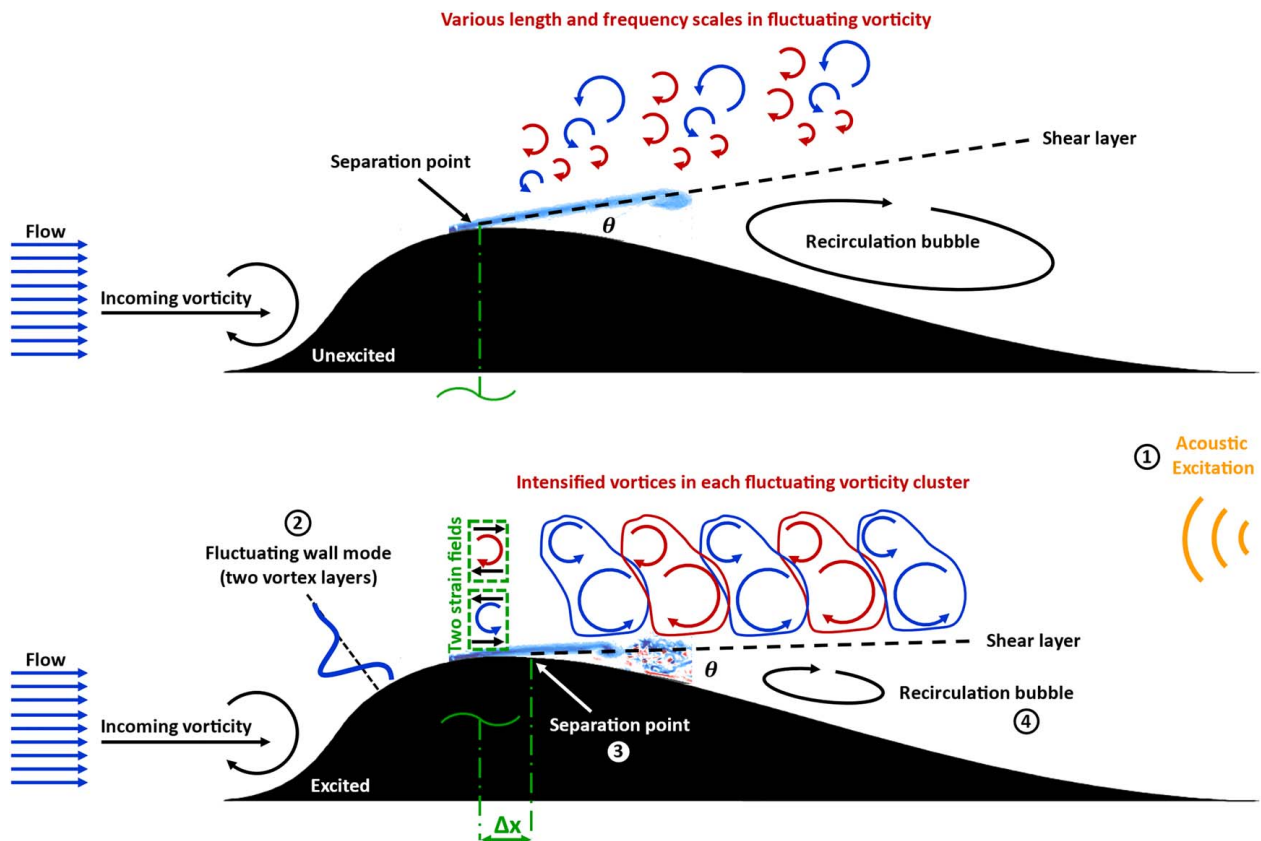


**Fig. 16  Mechanism of acoustic flow control**

point itself drives all of the flow modifications, which would mean that the unsteadiness signals should emanate in both directions from the separation point, contrary to the downstream directed signaling actually observed.

The temporal correlation analysis provides a means of sequentially describing the effect of acoustic actuation on the separation bubble and supports the hypothesis that the development of upstream wall modes is crucial to the regularization of the shear layer.

## 4 Discussion

The phase-averaging and correlation analyses identified the basic features of the acoustic actuation and their temporal sequence, which is illustrated in Fig. 16. The acoustic actuation first excited wall modes in the attached, upstream flow, resulting in a layered organization of the local vorticity distribution. The wall modes advect toward the separation point, where the organized vorticity tends to constrain the separating shear layer, causing it to bend closer to the wall, thereby contracting the size of the separation bubble. Evidence for the organized vorticity in the shear layer itself was found by the phase-averaged analysis. Once the separation bubble contracts, it reduces the blockage effect on the downstream side of the airfoil, thereby altering the pressure distribution in the outer flow, which ultimately results in an acceleration of the outer flow in the upstream region.

The accelerated attached flow therefore exhibits an intensified mean vorticity, as shown in Fig. 10, which in turn feeds into the developing wall modes. This process continues throughout the transient, for 15–20 cycles of perturbation itself. The correlation analysis provided the evidence for the sequential order of the transient behavior, as numbered in Fig. 16, and thus provided evidence in support of the hypothesis that upstream wall modes are essential in regularizing the separating shear layer.

The role of the wall modes may also explain the energetic advantage of acoustic forcing over direct actuation at the point of separation, as shown in Fig. 9. Introducing a small amplitude oscillatory disturbance to which the upstream flow field is receptive results in the natural generation of wall modes (of which Tollmien–Schlichting modes are the most-receptive/unstable form). These wall modes can then grow naturally, perhaps through transient growth mechanisms [47], extracting energy from the mean flow and directing it into the excitation frequency. In this way, the small input perturbation essentially exploits the natural receptivity of the flow to amplify its effect and exert a larger relative influence on the separation point than could be achieved with an equivalent input energy localized at the separation point itself.

The temporal scaling of the wall modes is, trivially, the same as the optimal actuation frequency scaling reported earlier, $(f\theta_s)/U_s \sim$ constant. The spatial scales of the wall modes are much longer than the usual T-S wavelength. Spatial wavenumbers ($\alpha\delta$, where $\alpha$ and $\delta$ are dimensional wavenumber and boundary thickness scale, respectively) of these wall modes are low ($\leq\pi/5$, calculated based on the field of view of the present experiments). $\alpha\delta$ of T-S mode, for example, in the attached region of the present flow would be $\approx 2\pi$, whereas the wavenumber of the observed wall modes was at least an order of magnitude smaller.

Static pressure measurements confirmed the scaling of the conducive acoustic excitation Strouhal number identical to that of the KH mode. From the detailed PIV measurements, it was ascertained that the acoustic waves generate the wall mode, which couple with the KH of the separated shear layer, thereby providing an alternative, but correct, explanation of the $St_{opt} \sim \sqrt{Re}$. Additionally, a higher amplitude of oscillations would result in a stronger wall mode, thereby affecting the shear layer KH mode more effectively, which is also consistent with the observations from the static pressure measurements.

## 5 Conclusion

As a global flow control methodology, the acoustic excitations offer an alternative to the more common direct localized actuation of airfoil separation, with potentially significant energy advantages. Two sets of experiments were performed to analyze the impact of acoustic excitation on a variety of geometries that approximate the physics representative of high work and lift airfoils observed in modern turbine airfoils. First, the effect of acoustic actuation on lift enhancement was quantified, and then the physical mechanisms generating this enhancement were explained. The hump surface pressure measurements showed a substantial increase in peak suction pressure, and the associated lift enhancement with acoustic excitation. The impact improved with increasing amplitude, and was optimal at a frequency close to the natural KH frequency of the separating shear layer. Full-field velocity measurements by PIV, when analyzed by phase-averaging and spatio-temporal correlation, revealed that the source of the change in the separation behavior was the presence of upstream wall modes, in the attached flow.

By energizing these wall modes, the acoustic excitation can exploit the natural receptivity of the boundary layer to organize the near-wall turbulence and thereby regularize the shear layer, resulting in a reduction of the separation bubble size. This new evidence in support of the causal importance of wall modes in influencing separation has implications for the design of future control schemes that can focus more narrowly on the optimization of the wall mode structure for improved performance.

Using active flow control techniques based on acoustic forcing was found to have the potential to significantly enhance airfoil performance at low Reynolds numbers. If successfully applied to the blades that were used to guide the development of the humps in this study, the implementation of acoustic flow control in a future engine prototype could result in substantial benefits for both the power plant and the overall unmanned air vehicle system. On the engine side, as much as a 15% reduction in weight is possible. This is accomplished by reducing the stage count, the airfoil count of the LPT module, and the overall engine length by 1, 57%, and 8 cm, respectively. These engine benefits carry through to an analysis of the aircraft system where there is the potential to increase either both the range and therefore the endurance by 10% or the absolute ceiling by 0.8 km.

## Conflict of Interest

There are no conflicts of interest.

## Data Availability Statement

The datasets generated and supporting the findings of this article are obtainable from the corresponding author upon reasonable request.

## Appendix

The nondimensional phase-averaged fluctuating vorticity is shown with Fig. 17 for six different phases at the excitation Strouhal number of 8.7 and Reynolds number of 46,000.
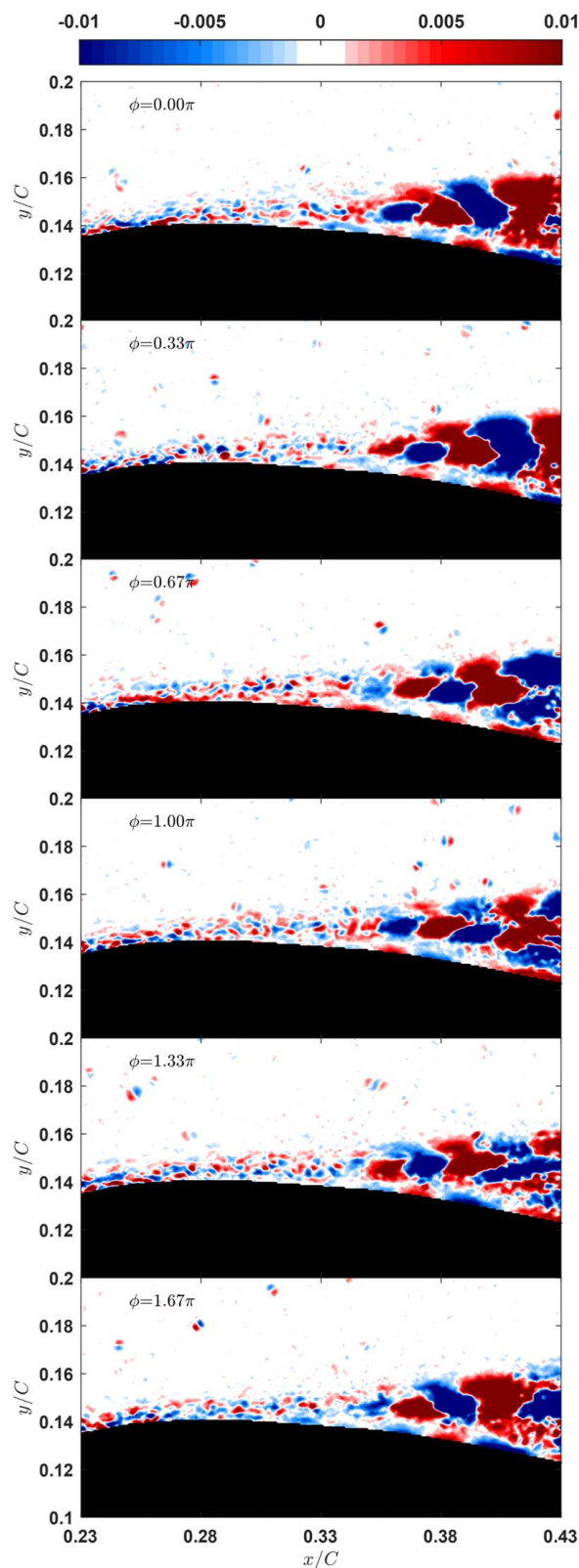
**Fig. 17. Phase-averaged fluctuating nondimensional vorticity shown at six different phases**

## References

[1] Seifert, A., Eliahu, S., Greenblatt, D., and Wygnanski, I., 1998, "Use of Piezoelectric Actuators for Airfoil Separation Control," AIAA J., **36**(8), pp. 1535–1537.

[2] Greenblatt, D., and Wygnanski, I. J., 2000, "Control of Flow Separation by Periodic Excitation," Prog. Aerosp. Sci., **36**(7), pp. 487–545.

[3] Seifert, A., and Pack, L. G., 1999, "Oscillatory Control of Separation at High Reynolds Numbers," AIAA J., **37**(9), pp. 1062–1071.

[4] Naveh, T., Seifert, A., Tumin, A., and Wygnanski, I., 1998, "Sweep Effect on Parameters Governing Control of Separation by Periodic Excitation," J Aircr, **35**(3), pp. 510–512.

[5] Greenblatt, D., Göksel, B., Rechenberg, I., Schüle, C. Y., Romann, D., and Paschereit, C. O., 2008, "Dielectric Barrier Discharge Flow Control at Very Low Flight Reynolds Numbers," AIAA J., **46**(6), pp. 1528–1541.

[6] Zhang, W., and Samtaney, R., 2015, "A Direct Numerical Simulation Investigation of the Synthetic Jet Frequency Effects on Separation Control of Low-Re Flow Past an Airfoil," Phys. Fluids, **27**(5), p. 055101.

[7] Collins, F. G., and Zelenevitz, J., 1975, "Influence of Sound upon Separated Flow Over Wings," AIAA J., **13**(3), pp. 408–410.

[8] Ahuja, K. K., 1985, "Some Unique Experiments on Receptivity," AIAA, **53**(9), pp. 1689–1699.

[9] Rice, E. J., and Zaman, K. B. M. Q., 1987, "Control of Shear Flows by Acoustic Excitation," AIAA 11th Aeroacoustics Conference, Sunnyvale, CA, Oct. 19–21.

[10] Zaman, K. B. M. Q., 1992, "Effect of Acoustic Excitation on Stalled Flows Over an Airfoil," AIAA J., **30**(6), pp. 1492–1499.

[11] Ahuja, K. K., Whipkey, R. R., and Jones, G. S., 1983, "Control of Turbulent Boundary Layer Flows by Sound," AIAA 8th Aeroacoustics Conference.

[12] Schubauer, G. B., and Skramstad, H. K., 1947, "Laminar Boundary-Layer Oscillations and Transition on a Flat Plate," J. Res. Natl. Inst. Stand., **38**(2), p. 251.

[13] Zaman, K. B. M. Q., Bar-Sever, A., and Mangalam, S. M., Sep. 1987, "Effect of Acoustic Excitation on the Flow Over a Low-Re Airfoil," J. Fluid Mech., **182**(1), p. 127–148.

[14] Ahuja, K. K., and Burrin, R. H., 1984, "Control of Flow Separation by Sound," AIAA 9th Aeroacoustics Conference, Williamsburg, VA, Oct. 10–15, pp. 1–14.

[15] Zaman, K. B. M. Q., McKinzie, D. J., and Rumsey, C. L., 1989, "A Natural Low-Frequency Oscillation of the Flow Over an Airfoil Near Stalling Conditions," **202**(403), pp. 403–442.

[16] Zaman, K. B. M. Q., and McKinzie, D. J., 1991, "Control of Laminar Separation Over Airfoils by Acoustic Excitation," AIAA J., **29**(7), pp. 1075–1083.

[17] Nishioka, M., Asai, M., and Yoshida, S., 1990, "Control of Flow Separation by Acoustic Excitation," AIAA J., **28**(11), pp. 1909–1915.

[18] Benton, S., and Bons, J. P., 2012, "The Effect of Acoustic Excitation on Boundary Layer Separation of a Highly Loaded LPT Blade," Proceedings of the ASME Turbo Expo, Cophenhagen, Denmark, June 11–15, pp. 1–11.

[19] Bernardini, C., Benton, S. I., and Jeffrey, P. B., 2013, "The Effect of Acoustic Excitation on Boundary Layer Separation of a Highly Loaded LPT Blade," ASME J. Turbomach., **135**(3), p. 051001.

[20] Tam, C. K. W., 1981, "The Excitation of Tollmien-Schlichting Waves in Low Subsonic Boundary Layers by Free-Stream Sound Waves," J. Fluid Mech., **109**, pp. 483–501.

[21] Goldstein, M. E., 1983, "The Evolution of Tollmien—Schlichting Waves Near a Leading Edge," J. Fluid Mech., **129**(1), pp. 443–453.

[22] Lam, S. H., and Rott, N., 1993, "Eigen-functions of Linearized Unsteady Boundary Layer Equations," ASME J. Fluids Eng., **115**(4), pp. 597–602.

[23] Goldstein, M. E., 1985, "Scattering of Acoustic Waves Into Tollmien-Schlichting Waves by Small Streamwise Variations in Surface Geometry," J. Fluid Mech., **154**, pp. 509–529.

[24] Pröbsting, S., and Yarusevych, S., 2021, "Airfoil Flow Receptivity to Simulated Tonal Noise Emissions," Phys. Fluids, **33**(4), pp. 1–16.

[25] Arbey, H., and Bataille, J., 1983, "Noise Generated by Airfoil Profiles Placed in a Uniform Laminar Flow," J. Fluid Mech., **134**, pp. 33–47.

[26] Pröbsting, S., and Yarusevych, S., 2015, "Laminar Separation Bubble Development on an Airfoil Emitting Tonal Noise," J. Fluid Mech., **780**, pp. 167–191.

[27] Bernardini, C., Benton, S. I., Lee, J. D., Bons, J. P., Chen, J., and Martelli, F., 2014, "Steady VGJ Flow Control on a Highly Loaded Transonic LPT Cascade: Effects of Compressibility and Roughness," Turbo Expo: Power for Land, Sea, and Air, Dusseldorf, Germany, June 16–20, pp. 1–14.

[28] Agarwal, T., Stratmann, M., Julius, S., and Cukurel, B., 2021, "Exploring Applicability of Acoustic Heat Transfer Enhancement Across Various Perturbation Elements," ASME J. Turbomach., **143**(3), p. 031001.

[29] Schmitz, J. T., et al., 2015, "Highly Loaded Low-Pressure Turbine: Design, Numerical, and Experimental Analysis," J. Propul. Power, **32**(1), pp. 142–152.

[30] Nowak, H. D., Luesma-Rodriguez, F., Rahbari, I., Clark, J. P., and Paniagua, G., 2023, "Response of Separated Boundary Layers to Steady and Pulsated Flow Injection," ASME J. Turbomach., **145**(6), p. 061001.

[31] Clark, J., Paniagua, G., and Cukurel, B., 2023, "On the Development of High Lift, High Work Low-Pressure Turbines," Proceedings of the ASME Turbo Expo.

[32] Gaster, M., 1967, "The Structure and Behaviour of Laminar Separation Bubbles," Aeronaut. Res. Council Rep. Mem., **3595**, pp. 1–31.

[33] Horton, H. P., 1968, *Laminar Separation Bubbles in Two and Three Dimensional Incompressible Flow*, Queen Mary College, London, UK.

[34] Gaster, M., 2004, "Laminar Separation Bubbles," IUTAM Symposium on Laminar-Turbulent Transition, Bangalore, India.

[35] Diwan, S. S., and Ramesh, O. N., 2009, "On the Origin of the Inflectional Instability of a Laminar Separation Bubble," J. Fluid Mech., **629**, pp. 263–298.

[36] Bendat, J. S., and Piersol, A. G., 1986, *Random Data, Analysis and Measurement Procedures*, John Wiley & Sons, New York.

[37] Holman, J. P., 2011, *Experimental Methods for Engineers*, 8th ed., McGraw-Hill, New York.

[38] Wieneke, B., Jul. 2015, "PIV Uncertainty Quantification From Correlation Statistics," Meas. Sci. Technol., **26**(7), p. 074002.

[39] Benedict, L. H., and Gould, R. D., 1996, "Towards Better Uncertainty Estimates for Turbulence Statistics," Exp. Fluids, **22**(2), pp. 129–136.

[40] Dovgal, A. V., Kozlov, V. V., and Michalke, A., 1994, "Laminar Boundary Layer Separation: Instability and Associated Phenomena," Prog. Aeros. Sci., **30**(1), pp. 61–94.

[41] Lachmann, G. V., 1955, "Boundary Layer Control," Aeronaut. J., **59**, pp. 163–198.

[42] Chang, R. C., Hsiao, F. B., and Shyu, R. N., 1992, "Forcing Level Effects of Internal Acoustic Excitation on the Improvement of Airfoil Performance," J. Aircraft, **29**(5), pp. 823–829.

[43] Seifert, A., Darabi, A., and Wygnanski, I., 1996, "Delay of Airfoil Stall by Periodic Excitation," J. Aircr., **33**(4), pp. 691–698.

[44] Smith, D. R., Amitay, M., Kibens, V., Parekh, D., and Glezer, A., 1998, "Modification of Lifting Body Aerodynamics Using Synthetic jet Actuators," 36th AIAA Aerospace Sciences Meeting and Exhibit.

[45] Li, S., Luo, Z., Deng, X., Liu, Z., Gao, T., and Zhao, Z., 2022, "Lift Enhancement Based on Virtual Aerodynamic Shape Using a Dual Synthetic Jet Actuator," Chin. J. Aeronaut., **35**(12), pp. 117–129.

[46] Jones, L. E., Sandberg, R. D., and Sandham, N. D., 2010, "Stability and Receptivity Characteristics of a Laminar Separation Bubble on an Aerofoil," J. Fluid Mech., **648**, pp. 257–296.

[47] Schoppa, W., and Hussain, F., 2002, "Coherent Structure Generation in Near-Wall Turbulence," J. Fluid Mech., **453**, pp. 57–108.